One-Pot Method Synthesis of Bimetallic MgCu-MOF-74 and Its CO$_2$ Adsorption under Visible Light

Jie Ling, Anning Zhou,* Wenzhen Wang,* Xinyu Jia, Mengdan Ma, and Yizhong Li

Cite This: *ACS Omega* 2022, 7, 19920−19929
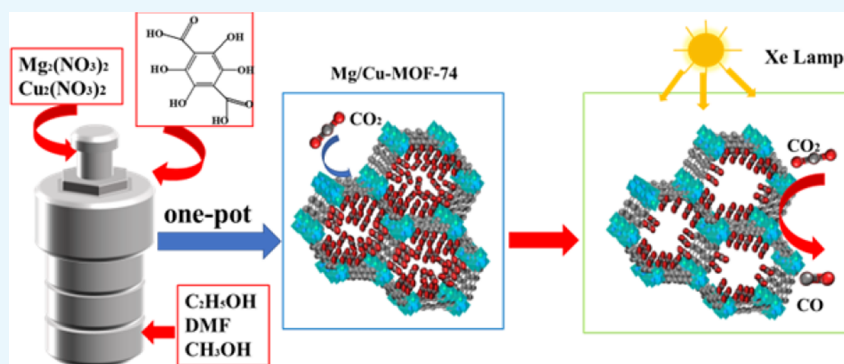
Read Online

ACCESS | 📊 Metrics & More | 📖 Article Recommendations | 🔵 Supporting Information

ABSTRACT: A magnesium-based metal−organic framework (Mg-MOF-74) exhibits excellent CO$_2$ adsorption under ambient conditions. However, the photostability of Mg-MOF-74 for CO$_2$ adsorption is poor. In this study, Mg$_x$Cu$_{1−x}$-MOF-74 was synthesized by using a facile "one-pot" method. Furthermore, the effects of synthesis conditions on the CO$_2$ adsorption capacity were investigated comprehensively. X-ray diffraction, Fourier transform infrared, scanning electron microscopy, thermo gravimetric analysis, inductively coupled plasma atomic emission spectroscopy, ultraviolet−visible spectroscopy and photoluminescence spectroscopy, and CO$_2$ static adsorption−desorption techniques were used to characterize the structures, morphology, and physicochemical properties of Mg$_x$Cu$_{1−x}$-MOF-74. CO$_2$ uptake of Mg$_x$Cu$_{1−x}$-MOF-74 under visible light illumination was measured by the CO$_2$ static adsorption test combined with the Xe lamp. The results revealed that Mg$_x$Cu$_{1−x}$-MOF-74 exhibited excellent photocatalytic activity. Furthermore, the CO$_2$ adsorption capacity of Mg$_x$Cu$_{1−x}$-MOF-74 was excellent at a synthesis temperature and time of 398 K and 24 h in dimethylformamide (DMF)-EtOH-MeOH mixing solvents, respectively. Mg$_x$Cu$_{1−x}$-MOF-74 retained a crystal structure similar to that of the corresponding monometallic MOF-74, and its CO$_2$ uptake under visible light was superior to that of the corresponding monometallic MOF-74. Particularly, the CO$_2$ uptake of Mg$_{0.4}$Cu$_{0.6}$-MOF-74 under Xe lamp illumination for 24 h was the highest, up to 3.52 mmol·g$^{−1}$, which was 1.18 and 2.09 times higher than that of Mg- and Cu-MOF-74, respectively. The yield of the photocatalytic reduction of CO$_2$ to CO was 49.44 μmol·g$_{cat}$$^{−1}$ over Mg$_{0.4}$Cu$_{0.6}$-MOF-74 under visible light for 8 h. Mg^{2+} and Cu^{2+} functioned as open alkali metal that could adsorb and activate CO$_2$. The synergistic effect between Mg and Cu metal strengthened Mg$_x$Cu$_{1−x}$-MOF-74 photostability for CO$_2$ adsorption and broadened the scope of its photocatalytic application. The "bimetallic" strategy exhibits considerable potential for use in MOF-based semiconductor composites and provides a feasible method for catalyst design with remarkable CO$_2$ adsorption capacity and photocatalytic activity.

INTRODUCTION

Metal−organic framework (MOF) materials, featuring highly effective structures (i.e., ultrahigh surface areas, extraordinary porosity, a highly ordered porous structure, and homogeneous active sites), exhibit considerable potential for use in carbon capture[1−3] and sequestration[4−6] (CCS) and heterogeneous catalysis,[7−9] especially in photocatalysis.[10−12] Among the numerous MOFs, Mg-MOF-74 (or CPO-27) exhibits the best CO$_2$ uptake in low pressures because of its open metal sites.[13,14] Yazaydin et al. analyzed the CO$_2$ adsorption capacities of M-MOF-74 (M = Ni, Zn, Co, and Mg) with simulation and experimental methods at 1 bar and 298 K and proved that the CO$_2$ uptake of Mg-MOF-74 was highest, up to

8 mmol·g$^{−1}$.[15] Bao et al. proved that the CO$_2$ uptake of Mg-MOF-74 was considerably higher than that of zeolite 13X, up to 8.61 mmol·g$^{−1}$. Mg-MOF-74 exhibits open metal sites. Compared with Na$^+$ in zeolite 13X, unsaturated Mg^{2+} has a smaller ionic radius and a larger ionic valence, which results in

stronger adsorbate–metal interactions.[16] MOFs with excellent CO_2 adsorption capacity have been used as co-catalysts in semiconductor composites for CO_2 photocatalytic reduction.[17,18] Zhao et al. reported a novel strategy for incorporating Mg-MOF-74 as a co-catalyst to prepare Zn_2GeO_4/Mg-MOF-74 and revealed that the CO_2 photocatalytic reduction of the semiconductor composites was considerably higher than that of single semiconductor materials. The productive rate of CO (12.94μ mol·g_{cat}^{-1}) was 7 times higher than that of Zn_2GeO_4 (1.8μmol·g_{cat}^{-1}).[19] The high concentration of open alkaline metal (Mg^{2+}) of Mg-MOF-74 was beneficial to the CO_2 adsorption and activation, which improved electron transfer from Zn_2GeO_4 to Mg-MOF-74 and effectively inhibited the excited electron–hole recombination of composites. Wang et al. revealed that Mg-MOF-74 (CPO-27)/TiO_2 exhibited enhanced photocatalytic reduction of CO_2 to CO and CH_4. Furthermore, Mg-MOF-74 exhibited excellent CO_2 adsorption capacity and open alkaline metal sites, which enhanced the photocatalytic performance of the composites.[20] Furthermore, although the CO_2 uptake of the Cu-based MOF was lower than that of Mg-MOF-74, the semiconductor composite of the Cu-based MOF exhibited excellent CO_2 photocatalytic reduction and physicochemical stability. Li et al. prepared a $Cu_3(BTC)_2$@TiO_2 semiconductor composite, and the yield of photocatalytic reduction of CO_2 to CH_4 was up to 2.64 μmol·g_{cat}^{-1}·h^{-1}. $Cu_3(BTC)_2$ functioned as a co-catalyst for $Cu_3(BTC)_2$@TiO_2 that exhibited excellent stability of the morphology and compositions after CO_2 photocatalytic reduction.[21] A strategy using Mg-MOFs as a co-catalyst and with excellent CO_2 adsorption capacity is required to enhance the photocatalytic performance of composite semiconductors.[22] However, the CO_2 uptake of Mg-MOF-74 is poor under ambient conditions. The existing studies of Mg-MOF-74 showed improved CO_2 uptake under humid conditions (i.e., water stability of CO_2).[23,24] The CO_2 uptake of Mg-MOF-74 under long-time illumination (i.e., photostability of CO_2) is yet to be discussed.

In bimetallic MOFs, two inorganic metal nodes are used to integrate two monometallic MOFs. Bimetallic MOFs considerably outperform their corresponding monometallic MOFs.[25−27] Although bimetallic Mg-MOF-74 is widely used in thermocatalysis[28,29] and adsorption,[30,31] its use in CO_2 photocatalytic reduction is limited.[32] Guo et al. prepared bimetallic NiMg-MOF-74 catalysts by using a solvothermal method and revealed that CO_2 can be photocatalytically reduced into formate over NiMg-MOF-74 under extremely harsh flue gas conditions. Furthermore, the excellent stability of NiMg-MOF-74 in the photocatalytic reaction was demonstrated through five cyclic photocatalytic experiments and X-ray diffraction (XRD) patterns after the photocatalytic reaction.[32] Consequently, based on the good CO_2 uptake of Mg-MOF-74 and the photostability of the Cu-based MOF, a bimetallic strategy was proposed to strengthen Mg-MOF-74 photostability for CO_2 adsorption.

We used the one-pot method to prepare a series of bimetallic $Mg_xCu_{1−x}$-MOF-74 (x = 0.4, 0.2, and 0.17). The effects of the preparation conditions (i.e., temperatures, time, and solvents) and Mg/Cu molar ratio on CO_2 adsorption were discussed. The relationship between the structure and CO_2 adsorption under visible light illumination was investigated through inductively coupled plasma atomic emission spectroscopy (ICP-AES), XRD, Fourier transform infrared (FT-IR), scanning electron microscopy (SEM), thermo gravimetric

analysis (TGA), and density functional theory (DFT). The photocatalytic performance of the MgCu-MOF was verified. In this study, an executable and competitive method was proposed for design of MOF-based semiconductor composites for excellent CO_2 adsorption capacity and considerable photocatalytic activity.

■ MATERIALS AND EXPERIMENT

Materials. All organic and inorganic chemicals in this study were of commercially available analytical grade and were used without further purification. Magnesium nitrate hexahydrate [$Mg(NO_3)_2$·$6H_2O$, 99.0%] and copper nitrate hydrate [$Cu(NO_3)_2$·$3H_2O$, 99.0%] were purchased from Kermel. 2,5-Dihydroxyterephthalic acid (H_4dhtp, 98.0%) and N,N-dimethylformamide (DMF, 99.8%) were purchased from Macklin. Anhydrous ethanol (EtOH, 99.7%), anhydrous methanol (MeOH, 99.8%), and 2-propanol (IPA, 99.7%) were purchased from Fuyu Fine Chemical Co., Ltd. (Tianjin, China).

Characterization. The crystal structure was identified using an X-ray diffractometer (7000S/L, Shimadzu) with Cu Kα radiation. The morphology was observed using a scanning electron microscope (S-4800, Hitachi) with a magnification of 2000−20,000 times and an acceleration voltage of 5 kV. The chemical structure and functional groups were determined using a FT-IR spectroscope (Tensor 27, Bruker); each spectrum was obtained from the acquisition of 32 scans from 4000 to 400 cm^{-1} with 2 cm^{-1}. Thermogravimetry and derivative thermogravimetry (Mettler Toledo) were performed using a TGA analyzer. Elemental quantitative analysis was performed using an inductively coupled high-frequency plasma emission spectrometer (715-ES, Agilent). Before the test, the sample was dissolved completely with concentrated nitric acid and subsequently diluted to 250 mL with ultrapure water. The band gap width was measured using an ultraviolet−visible spectrophotometer (UV-2600, Shimadzu). The photoluminescence (PL) spectra were recorded on a fluorescence spectrophotometer (PL, F-4600, Hitachi). The excitation wavelength was set to 370−580 nm. The pore structures were determined by N_2 adsorption−desorption isotherms at 77 K using the Micromeritics ASAP 2460 adsorption apparatus. All samples were as-treated by heating at 473 K for 10 h in a dynamic vacuum before measurement. The surface area and micropore diameter were calculated through DFT. Micropore volume and average micropore diameter were calculated using the Horvath−Kawazoe (H−K) method.

Synthesis of $Mg_xCu_{1−x}$-MOF-74. To obtain $Mg_xCu_{1−x}$-MOF-74, $Mg(NO_3)_2$·$6H_2O$ and $Cu(NO_3)_2$·$3H_2O$ were mixed in the molar ratio of 2:1 ($Mg_{0.67}Cu_{0.33}$), 1.5:1.5 ($Mg_{0.5}Cu_{0.5}$), and 1:2 ($Mg_{0.33}Cu_{0.67}$). Next, the synthesis method of $Mg_xCu_{1−x}$-MOF-74 (x = 0.67, 0.5, and 0.33) was consistent with the synthesis of Mg-MOF-74 and Cu-MOF-74. Furthermore, $Mg_{0.5}Cu_{0.5}$-MOF-74 was synthesized at the three temperatures (398, 408, and 418 K), at three times (12, 24, and 36 h), and in three solvents (A, B, and C). A is DMF-MeOH-EtOH, B is DMF-EtOH-IPA, and C is DMF-MeOH-IPA.

CO_2 Adsorption Measurement. The CO_2 static adsorption−desorption isotherms of activated samples were obtained using the Micromeritics ASAP 2460 adsorption apparatus, which were measured at 298 K and gas pressure up to 760 mm Hg. The temperature control system was achieved
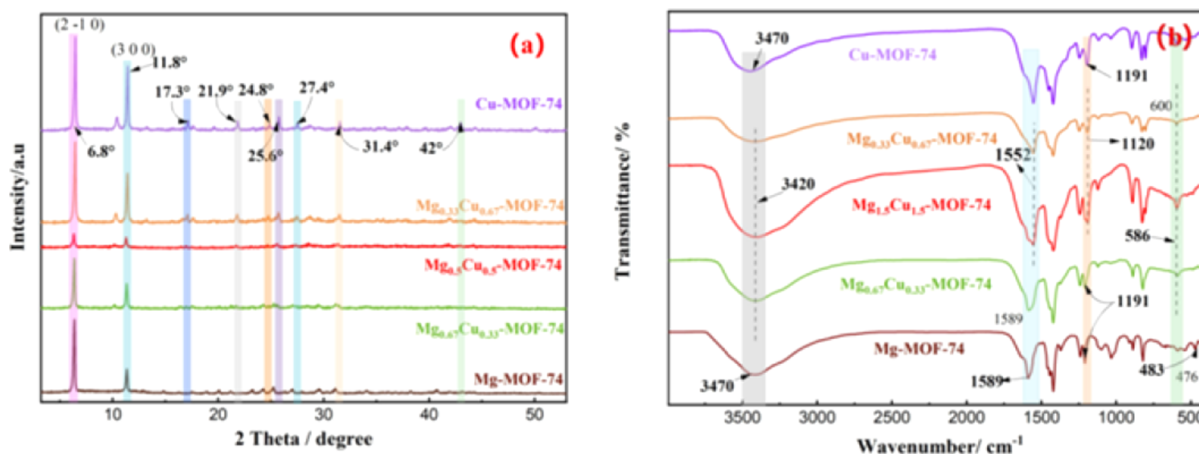
Figure 1. (a) Powder XRD patterns and (b) FT-IR spectra of Mg-, Cu-MOF-74, and Mg_xCu_{1-x}-MOF-74.

using a Dewar bottle with a circulating sleeve connected to a thermostatic bath.

Photostability of Mg_xCu_{1-x}-MOF-74 for CO_2 Adsorption Measurement. The activated samples were treated using a Xe lamp (CEL-HXL300, China Education Au-Light Co., Ltd., Beijing) at three times (12, 24, and 36 h), and the CO_2 uptake was evaluated. The test method was the same.

Photocatalytic Activity of Mg_xCu_{1-x}-MOF-74 for CO_2 Measurement. A 300 W Xe lamp was used as the visible light. The samples (20 mg) and deionized water (2 mL) were both placed in a closed reactor (CEL-HPR100T) with a sapphire window and temperature control system. Before the reaction, the reactor was blown with pure CO_2 with a flow rate of 20 mL·min^{-1} for 15 min to ensure elimination of all air. The pressure and temperature of the sealed reaction system were increased to 1 MPa and 150 °C, respectively, and stirred in the dark for 30 min to ensure that the catalysts reached the adsorption−desorption equilibrium. After a certain time, the gases produced were analyzed and quantified through BFRL SP-3510 gas chromatography (GC) and quantified with a TCD and FID.

■ RESULTS AND DISCUSSION

Metal Composition Measurement of As-Prepared Samples. To confirm the metal composition of samples, ICP-AES analyses were conducted (Table S1). According to the ICP-AES results, Mg and Cu coexist in Mg_xCu_{1-x}-MOF-74. With the increase in the Cu content, the Mg/Cu molar ratio decreased. The results are consistent with the experimental system and proved that Mg_xCu_{1-x}-MOF-74 with various Mg/Cu metal ratios can be synthesized. However, the Cu content in the Mg_xCu_{1-x}-MOF-74 structure was considerably higher than the Mg content. This phenomenon can be attributed to the higher stability of Cu-MOF-74 than that of Mg-MOF-74. Cu is more easily coordinated with the H_4dhtp to form MOF-74 than Mg, and the synthesis temperature of Cu-MOF-74 (353 K) is lower than that of Mg-MOF-74 (398 K).[33,34] Therefore, Cu-MOF-74 is preferentially formed in the synthesis process of Mg_xCu_{1-x}-MOF-74, and Mg^{2+} replaces part of Cu^{2+} into the lattice. Because Cu−O bond length is longer than that of the Mg−O bond, the coordination of the Mg_xCu_{1-x}-MOF is distorted and deformed because of the Jahn−Teller effect.[35] The coordination distortion affects the synthesis of Mg_xCu_{1-x}-MOF-74, which

results in a lower Mg content than Cu. The result is consistent with TG analysis mentioned previously.

According to ICP-AES analysis, the Mg/Cu metal ratio was adjusted to $Mg_{0.4}Cu_{0.6}$, $Mg_{0.2}Cu_{0.8}$, and $Mg_{0.17}Cu_{0.83}$. Furthermore, all structures and properties of Mg_xCu_{1-x}-MOF-74 in the study are discussed with reference to the adjusted Mg/Cu molar ratio.

Influence of Synthesis Conditions and the Mg/Cu Molar Ratio on the Crystal Structure and Morphology. The crystal structure of samples under four conditions of temperatures, time, solvents, and the metal molar ratio was confirmed through XRD (Figure S1). The XRD pattern of $Mg_{0.2}Cu_{0.8}$-MOF-74 under three conditions (temperatures, time, and solvents) exhibits two diffraction peaks at $2\theta = 6.8°$ and 11.8°, which correspond to the (210) and (300) crystal faces of Mg-MOF-74, respectively. Furthermore, the pattern is same as that of Mg-MOF-74.[27,36,37] A novel diffraction peak at $2\theta = 10.4°$ (Figure S1b) did not belong to MgO or CuO, which could be attributed to the impurity resulting from the coordination reaction of Mg, Cu, and DMF.[38] The XRD patterns of Mg_xCu_{1-x}-MOF-74 were well consistent with those of Mg- or Cu-MOF-74 (Figure 1a). Mg_xCu_{1-x}-MOF-74 revealed major diffraction peaks at $2\theta = 6.8°$, 11.8°, 17.3°, 21.9°, 24.8°, 25.6°, 27.4°, 31.4°, and 42°, which are consistent with those of reported MOF-74.[39,40] Replacing Mg with Cu does not affect the crystal structure of Mg-MOF-74, and Mg_xCu_{1-x}-MOF-74 is successfully synthesized.

FT-IR was performed to detect the surface functional groups of samples under four synthesis conditions of various temperatures, time, solvents, and metal molar ratios (Figure S1d−f). According to the coordination characteristics of the MOF, all vibrations can be distinguished into two distinctive regions.[41,42] The characteristic vibrations above the 700 cm^{-1} region are organic ligands and those below 700 cm^{-1} regions mainly belong to metal centers of Mg and Cu.[42] Several sharp and clear absorption peaks were observed at 1522, 1420, 890, and 823 cm^{-1}, which were ascribed to $\nu(-C=O)$, $\nu(-COO-)$, and $\nu(C-H)$ of benzene rings in H_4dhtp (Figure S1d).[28,42] The sharp and weak peak at 1240 cm^{-1} is attributed to the stretching vibration of the C−O band of the phenolate group. $Mg_{0.2}Cu_{0.8}$-MOF-74 obtained under various preparation conditions exhibits the aforementioned characteristic peaks (from Figure S1d−f),[38] which proves that $Mg_{0.2}Cu_{0.8}$-MOF-74 was successfully synthesized.
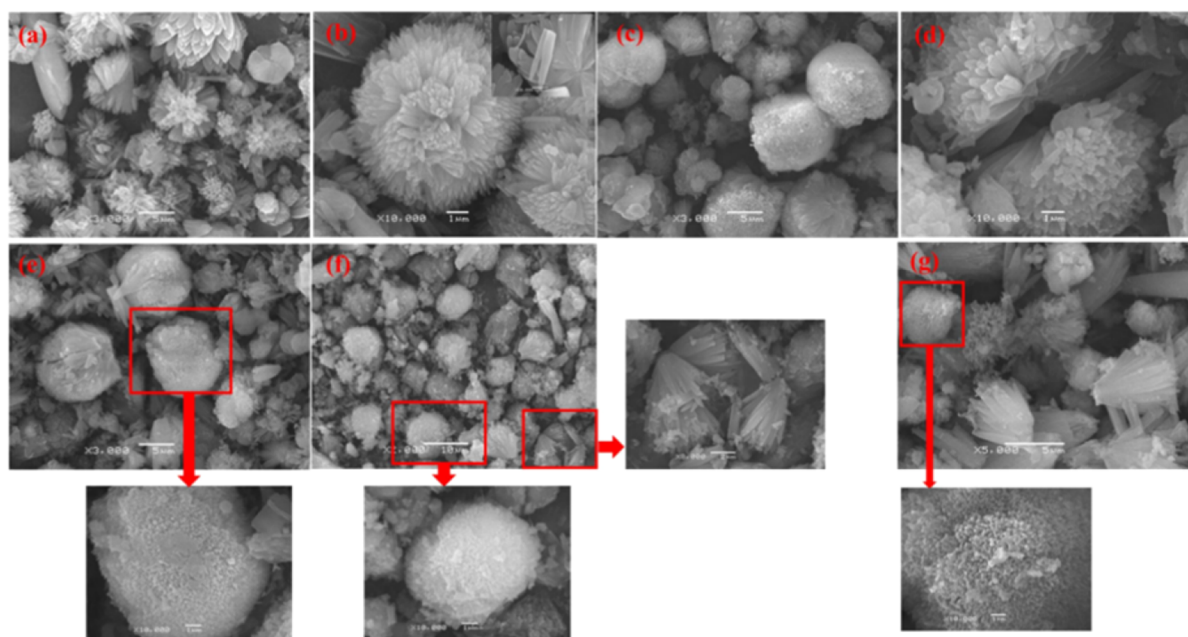
Figure 2. (a) SEM images of synthesized (b) Mg-, (g) Cu-, and (c,d) $Mg_{0.4}Cu_{0.6}$-; (e) $Mg_{0.2}Cu_{0.8}$-; and (f) $Mg_{0.17}Cu_{0.83}$-MOF-74.

Notably, the functional groups of $Mg_{0.2}Cu_{0.8}$-MOF-74 were primarily affected by the synthesis temperature and less affected by synthesis time and solvents. The characteristic peaks at 889 and 823 cm^{-1} of $Mg_{0.2}Cu_{0.8}$-MOF-74 nearly disappeared at a synthesis temperature of 145 °C, which indicated that the synthesis temperature affected the coordination reaction between metal ions and organic ligands (Figure S1d).[38] The Cu metal ratio of Mg_xCu_{1-x}-MOF-74 exceeded 50%, and the characteristic peaks of 1589 and 1191 cm^{-1} in the spectrum of Mg-MOF-74 transferred to 1552 and 1191 cm^{-1}, respectively (Figure 1b). This phenomenon is attributed to the conjugated effect of Mg_xCu_{1-x}-MOF-74. The C=O group conjugates with the C=C bond, and delocalization of the π-electrons occurred between two unsaturated bands. The double bond characteristics of C=O were reduced, which resulted in the shift of the absorption frequency toward a lower wave number.[36] Therefore, strongly coordinated olefin molecules existed in the metal centers of Mg_xCu_{1-x}-MOF-74.

The morphology and structures of samples at three synthesis temperatures (398, 408, and 418 K) were observed through SEM (Figure S2a). The morphology structure of Mg_xCu_{1-x}-MOF-74 was affected by synthesis temperature. Furthermore, $Mg_{0.2}Cu_{0.8}$-MOF-74 at 398 K exhibited a spherical crystal structure formed by the reaggregation of needle-like crystals in diameters less than approximately 1 μm (Figure S2a,b).[36] The morphology of $Mg_{0.2}Cu_{0.8}$-MOF-74 at 418 K exhibited flake crystal branches (Figure S2d). $Mg_{0.2}Cu_{0.8}$-MOF-74 at 408 K formed flake crystal branches (Figure S2c), which are slightly larger than the needle crystal branches of $Mg_{0.2}Cu_{0.8}$-MOF-74 at 398 K. The temperature can promote crystal growth; however, excessively high temperature leads to grain agglomeration.[43] With the increase in temperature, the dispersion degree of the attachment energy of each modified crystal surface increased, which resulted in various growth rates between the crystal surfaces.[44,45] The morphology of $Mg_{0.2}Cu_{0.8}$-MOF-74 at 418 °C was nonspherical. The morphology structure of Mg_xCu_{1-x}-MOF-74 was also affected

by the Mg/Cu molar ratio (Figure 2). Mg-MOF-74 exhibited a chrysanthemum-like morphology formed by polyhedral prism crystal branches (Figure 2a,b). The spherical structures of Cu-MOF-74 consisted of needle-like crystal branches, and the average crystal is less than 5 μm (from Figure 2c−f). With the increase in the Cu content, the petal structure of Mg_xCu_{1-x}-MOF-74 changed from prismatic petals to needle-like petals. Therefore, the average particle size of $Mg_{0.17}Cu_{0.83}$-MOF-74 with the lowest Mg/Cu molar ratio ($n_{Mg}/n_{Cu} = 0.20$) was close to 5 μm. Mg_xCu_{1-x}-MOF-74 with a hydrangea-like morphology exhibited a structure denser than that of the corresponding monometallic MOF-74, which results in its specific surface area becoming larger than that of Cu-MOF-74 and its thermal stability being superior to that of Mg-MOF-74.

Influence of the Mg/Cu Molar Ratio on Thermal Stability. Two main mass loss stages exist in the TG curves of Mg_xCu_{1-x}-MOF-74 in a N_2 atmosphere, which revealed the weight loss temperature of each sample (Figure 3a). The first mass loss stage started with heating and lasts until the start of the second stage at various temperatures. For Cu-MOF-74, the starting and finishing temperatures reduced to 308 and 475 °C, respectively. For Mg-MOF-74, the starting and finishing temperatures reduced to 267 and 609 °C, respectively. The mass loss temperatures of Mg_xCu_{1-x}-MOF-74 in the second stage were between those of Mg- and Cu-MOF-74. In the first stage, the mass loss was attributed to the removal of adsorbed water, gas molecules, and residual solvents, such as methanol, ethanol, or DMF.[27,46] The weightlessness in the second stage corresponds to the collapse of the framework structure, which disintegrated organic ligands and formed metal oxides.[35,47] The TG curve of Mg-MOF-74 reveals that the thermal stability of Mg-MOF-74 was not satisfied. However, the thermal stability of Mg_xCu_{1-x}-MOF-74 was enhanced considerably. The considerable difference in the thermostability of Mg_xCu_{1-x}-MOF-74 could be attributed to the synergy between Mg and Cu.[48] To avoid the structural collapse of Mg_xCu_{1-x}-MOF-74, its thermal treatments were strictly performed at less than 200 °C.
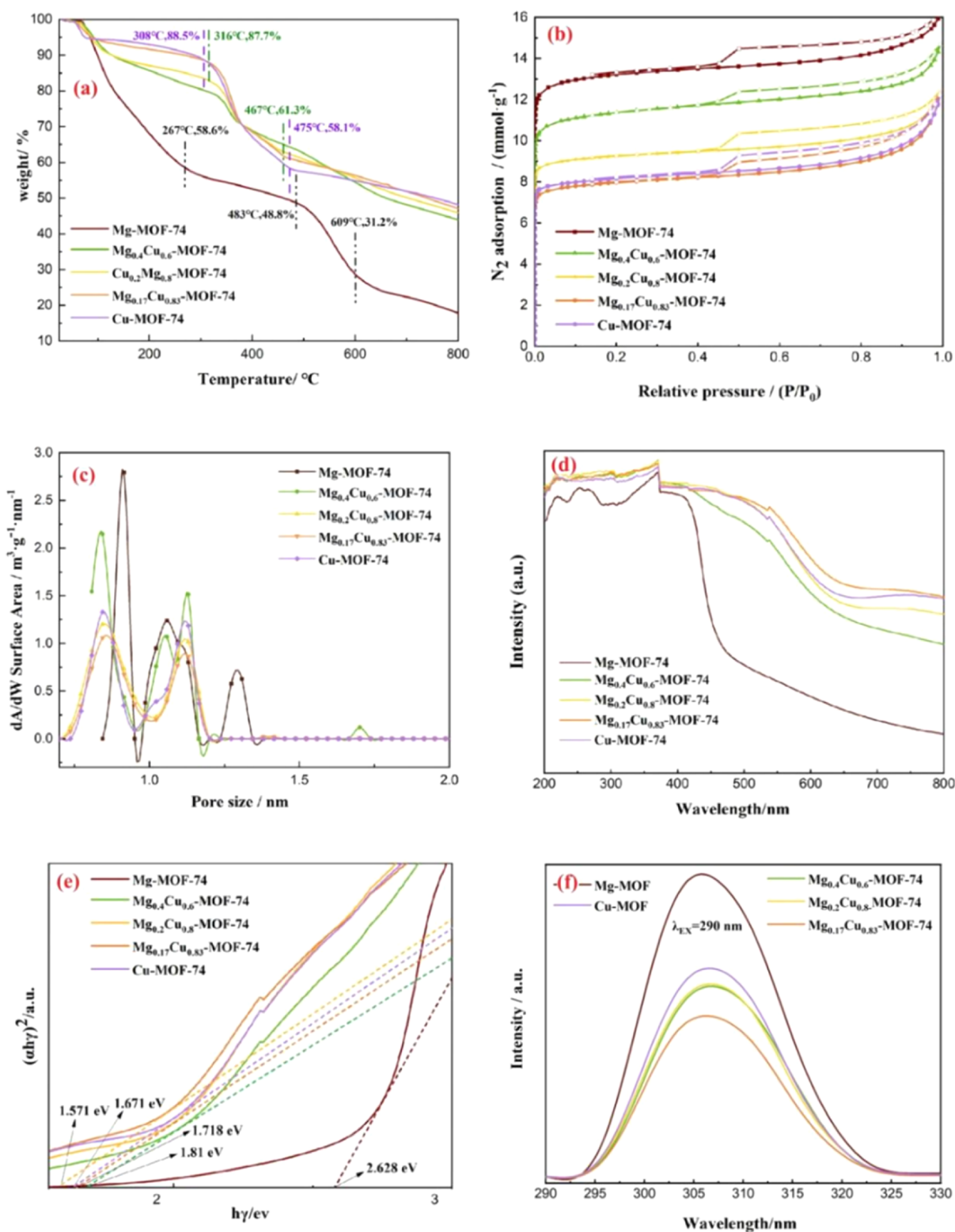
Figure 3. (a) TG (N_2 atmosphere), (b) N_2 adsorption−desorption isotherms, (c) pore size distribution curves, (d) UV−vis DRS, (e) E_g, and (f) PL spectra of Mg_xCu_{1-x}-MOF-74.

Influence of the Mg/Cu Molar Ratio on Pore Structures. To investigate the influence of the Mg/Cu molar ratio on the pore structures of Mg_xCu_{1-x}-MOF-74, N_2 adsorption−desorption isotherms of Mg-, Cu-, and Mg_xCu_{1-x}-MOF-74 at 77 K were measured (Figure 3b,c). Mg_xCu_{1-x}-MOF-74 exhibited a typical type I isotherm and type H$_3$

hysteresis loops, which indicated that both microporous and mesoporous structures were the same. The micropores of Mg_xCu_{1-x}-MOF-74 were predominantly between 0.84 and 1.70 nm, which is consistent with the previous report (Figure 3c).[24,36] The surface area of $Mg_{0.4}Cu_{0.6}$-MOF-74 calculated according to the DFT method was 1561.96 m^2·g^{-1}, which was

approximately 3.18% higher than that of Mg-MOF-74 and 50.96% higher than that of Cu-MOF-74 (Table 1). The

Table 1. Pore Structure Analyses of Mg_xCu_{1-x}-MOF-74

sample	total Area in pore[a], m^2/g	Langmuir specific surface area, m^2/g	micropore volume[b], cm^3/g	average pore size[b], nm
Mg-MOF-74	1513.75	1448	0.45	0.75
$Mg_{0.4}Cu_{0.6}$-MOF-74	1561.96	1278	0.39	0.77
$Mg_{0.2}Cu_{0.8}$-MOF-74	1235.0	1061	0.32	0.76
$Mg_{0.17}Cu_{0.83}$-MOF-74	1012.50	978	0.27	0.77
Cu-MOF-74	1034.58	989	0.28	0.77

[a]Total area in the pore calculated by the DFT method. [b]Micropore volume and average pore size calculated by the H−K method.

micropore volume of $Mg_{0.4}Cu_{0.6}$-MOF-74 calculated according to the H−K method is the highest among Mg_xCu_{1-x}-MOF-74 samples, at approximately 0.39 $cm^3 \cdot g^{-1}$. The surface area and micropore volume of $Mg_{0.17}Cu_{0.83}$-MOF-74 were the lowest. The surface area and micropore size of Mg_xCu_{1-x}-MOF-74 decreased with the increase in the Cu content, which is consistent with the results of the ICP-AES analysis.

Influence of the Mg/Cu Molar Ratio on Optical Properties. UV−vis spectra were analyzed to confirm the

optical performance of Mg_xCu_{1-x}-MOF-74 (Figure 3d). The absorption spectrum of Mg-MOF-74 exhibited a strong absorption in the wavelength range of 200−413 nm, and the light absorption decreased considerably in the visible region (above 420 nm). Light absorption capacities of Cu-MOF-74 and Mg_xCu_{1-x}-MOF-74 are better than those of Mg-MOF-74. Their absorption spectra revealed a stronger absorption in the wavelength range 200−530 nm but decreased slightly above 530 nm (Figure 3d). With the increase in the Cu content in Mg_xCu_{1-x}-MOF-74, its absorption band edges exhibited a red shift with enhanced visible light absorption. The light absorption capacity of Mg_xCu_{1-x}-MOF-74 was stronger than that of Cu-MOF-74 and Mg-MOF-74 in the UV region. However, the light absorption capacity of $Mg_{0.4}Cu_{0.6}$-MOF-74 and $Mg_{0.2}Cu_{0.8}$-MOF-74 was lower than that of Cu-MOF-74 in the visible region. The visible light absorption capacity of $Mg_{0.17}Cu_{0.83}$-MOF-74 above 480 nm was highest because the absorption spectrum of Cu-MOF-74 exhibited strong absorption in both UV and visible regions. Replacing the Mg of Mg-MOF-74 with Cu can enhance the light absorption capacity of Mg_xCu_{1-x}-MOF-74 in the visible region. Moreover, Cu and Mg exhibit distinct coordination structures with H_4dhtp in the process of synthesizing Mg_xCu_{1-x}-MOF-74, which affects their visible light absorption ability. The band gap energy (E_g) was calculated from the UV absorption spectrum
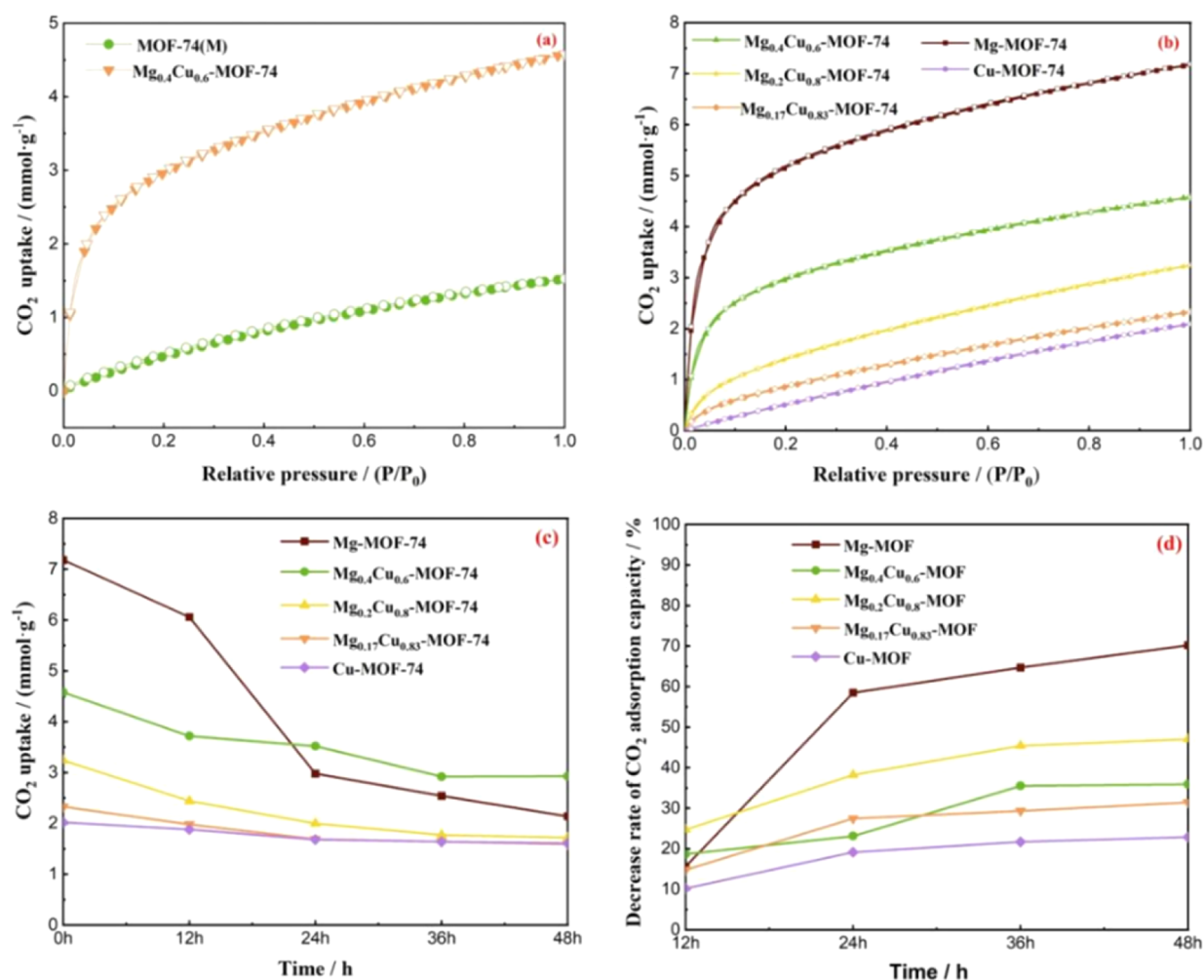

Figure 4. (a) CO_2 adsorption−desorption isotherms of $Mg_{0.4}Cu_{0.6}$- and MOF-74(M), (b) CO_2 adsorption−desorption isotherms of Mg_xCu_{1-x}- at 298 K and 1 bar, (c) CO_2 uptake of Mg_xCu_{1-x}- treated using the X-lamp for 12, 24, 36, and 48 h, and (d) CO_2 decrease rate of Mg_xCu_{1-x}-MOF-74.

of Mg_xCu_{1-x}-MOF-74. The Kubelka−Munk transformation spectra of Mg_xCu_{1-x}-MOF-74 were estimated, and the tangent line was drawn and calculated by using software. The results revealed that the E_g values of Mg-, $Mg_{0.4}Cu_{0.6}$-, $Mg_{0.2}Cu_{0.8}$-, $Mg_{0.17}Cu_{0.83}$-, and Cu-MOF-74 were 2.628, 1.810, 1.718, 1.571, and 1.671 eV, respectively (Figure 3e). The absorption band edge of Mg_xCu_{1-x}-MOF-74 exhibited a red shift with the decrease in E_g, and the visible light absorption was enhanced. Here, the E_g of $Mg_{0.17}Cu_{0.83}$-MOF-74 was the lowest, which was attributed to its highest response properties in visible light above 480 nm. The result revealed that replacing the Mg of Mg-MOF-74 with Cu can reduce the band gap and enhance the visible light response, which improves the photocatalytic activity.

PL emission spectroscopy was studied to verify the photocatalytic activity of Mg_xCu_{1-x}-MOF-74 (Figure 3f). The emission peaks of the PL spectra were attributed to the recombination of excited free carriers. The emission intensities of $Mg_{0.4}Cu_{0.6}$-, $Mg_{0.2}Cu_{0.8}$-, and $Mg_{0.17}Cu_{0.83}$-MOF-74 were all lower than those of Mg- and Cu-MOF-74. With the increase in Cu, the PL peak intensities of Mg_xCu_{1-x}-MOF-74 decreased considerably. Replacing the Mg of Mg-MOF-74 with Cu can inhibit the recombination of electron−holes and enhance photocatalytic activity because the lower intensity of PL indicates higher separation efficiency of electron−hole pairs, that is, the superior photocatalytic activity.[12,49,50]

Influence of Synthesis Conditions on CO_2 Adsorption Capacity. To confirm the effect of synthesis conditions on the CO_2 uptake of Mg_xCu_{1-x}-MOF-74, the CO_2 uptake of S at 298 K and 1 bar under three synthesis conditions (time, temperatures, and solvents) was tested (Table S2). The CO_2 uptake of S-398-24-A (i.e., 398 is temperature, 24 is time, and A is the solvent) was the highest, up to 3.24 mmol·g^{-1}. Thus, the best synthesis condition was 398 K, 24 h, and in A.

To verify that Mg_xCu_{1-x}-MOF-74 was successfully synthesized, we obtained the mechanical combination of two corresponding monometallic MOF-74 in a molar ratio of 2:1 and tested CO_2 uptake (Figure 4a). The CO_2 uptake of $Mg_{0.4}Cu_{0.6}$-MOF-74 outperformed that of the mechanically mixed MOF-74(M), which proved that Mg_xCu_{1-x}-MOF-74 was synthesized successfully. The synergistic effects originating from two adjacent Mg and Cu metals considerably improved the CO_2 adsorption capacity.[28]

Evaluation of the Photostability of Mg_xCu_{1-x}-MOF-74 for CO_2 Adsorption. To investigate the effect of the Mg/Cu molar ratio on the photostability of Mg_xCu_{1-x}-MOF-74 for CO_2 adsorption, the adsorption−desorption isotherms at 298 K and 1 bar were compared to those obtained by the static volumetric CO_2 adsorption method (Figure 4b). The CO_2 uptake of Mg_xCu_{1-x}-MOF-74 was higher than that of Cu-MOF-74 but lower than that of Mg-MOF-74. Specifically, the CO_2 uptake of $Mg_{0.4}Cu_{0.6}$-MOF-74 was the highest, up to 4.58 mmol·g^{-1}, and that of $Mg_{0.17}Cu_{0.83}$-MOF-74 was the lowest, up to 1.52 mmol·g^{-1}. This phenomenon could be attributed to the surface area and the pore volume of $Mg_{0.4}Cu_{0.6}$-MOF-74, which is consistent with the pore structure analysis. Moreover, the CO_2 adsorption capacity of Mg_xCu_{1-x}-MOF-74 was influenced by the Mg content. With the decrease in the Mg content, the CO_2 uptake of Mg_xCu_{1-x}-MOF decreased, which was attributed to the CO_2 adsorption heat of Mg ions being larger than that of Cu ions in a low-pressure region.[35]

To investigate the effect of the Mg/Cu molar ratio on chemical stability and photostability of Mg_xCu_{1-x}-MOF-74,

the CO_2 uptake of the Mg_xCu_{1-x}-MOF-74 treated using a Xe lamp was measured by using the static volumetric CO_2 adsorption method (Figure 4c). The CO_2 uptake of Mg_xCu_{1-x}-MOF-74 decreased with the increase in the illumination time, and the CO_2 uptake of those treated using an X-lamp for more than 24 h was the lowest and stable. Furthermore, the CO_2 uptake values of Mg-, $Mg_{0.4}Cu_{0.6}$-, $Mg_{0.2}Cu_{0.8}$- $Mg_{0.17}Cu_{0.83}$-, and Cu-MOF-74 treated by using the X-lamp for 24 h were 2.98, 3.52, 2, 1.69, and 1.68 mmol·g^{-1}, respectively. To analyze the effect of the Mg/Cu molar ratio on the photostability of Mg_xCu_{1-x}-MOF-74 for CO_2 adsorption, the decrease rate in the CO_2 uptake of those treated by the X-lamp for 12, 24, 36, and 48 h was quantitatively discussed (Figure 4c). The CO_2 uptake decrease rate (100%) of Mg_xCu_{1-x}-MOF-74 under long-term illumination is defined as follows

$$Y = \frac{C_n - C_0}{C_0} \times 100\%$$

(1)

Here, Y indicates the CO_2 decrease rate; C_n indicates the CO_2 uptake of Mg_xCu_{1-x}-MOF-74 treated using the X-lamp for 12, 24, 36, and 48 h; and C_0 indicates the CO_2 uptake of Mg_xCu_{1-x}-MOF-74.

Mg-MOF-74 treated using the X-lamp for 48 h exhibited the most severe decrease in CO_2 uptake, and the CO_2 uptake decrease rate was as high as 65.59%, which is approximately 3 times that of Cu-MOF-74 (22.90%). The CO_2 uptake decrease rate of Mg_xCu_{1-x}-MOF-74 treated using the X-lamp for 36 h reached photostability and that of $Mg_{0.4}Cu_{0.6}$-, $Mg_{0.2}Cu_{0.8}$-, and $Mg_{0.17}Cu_{0.83}$-MOF-74 was 29.34, 45.42, and 35.51%, respectively (Figure 4d). The CO_2 uptake of Mg-MOF-74 was the highest and reached 7.18 mmol·g^{-1}. However, its photostability was the weakest (Figure 4c,d). The photostability of Cu-MOF-74 for CO_2 uptake was the best. The CO_2 uptake of Cu-MOF-74 was the lowest, only up to 2.09 mmol·g^{-1}. Mg_xCu_{1-x}-MOF-74 photostability of CO_2 adsorption was superior to that of two corresponding monometallic MOF-74 (Figure 4c). Specifically, the photostability of $Mg_{0.4}Cu_{0.6}$-MOF-74 treated using the X-lamp for 24 h was the best, and its CO_2 uptake and decrease rate were 3.52 mmol·g^{-1} and 23.13%, respectively. A strong relationship exists between photostability and metal composition of Mg_xCu_{1-x}-MOF-74. Because of the synergistic effect between Cu and Mg, the photostability of Mg_xCu_{1-x}-MOF-74 was enhanced considerably.[32] Furthermore, the stability of Mg-MOF-74 was highly affected by the M−O bond on the top of the metal−organic frame (M represents the metal species) and the metal center atoms (Mg).[31] The distortion and deformation of the coordination environment of Cu^{2+} (i.e., Jahn−Teller effect) lead to the contraction of M−O bonds and improved photostability of Mg_xCu_{1-x}-MOF-74.[35]

Evaluation of the CO_2 Photocatalytic Activity of $Mg_{0.4}Cu_{0.6}$-MOF-74. To confirm the potential application of $Mg_{0.4}Cu_{0.6}$-MOF-74 as a co-catalyst for MOF-based semiconductor composites, its CO_2 photoreduction activity was investigated without any sacrificial agent (Table 2). The main gaseous product of CO_2 photoreduction in an aqueous system was CO. The yield of CO was 49.44 μmol·g_{cat}^{-1} over $Mg_{0.4}Cu_{0.6}$-MOF-74 under visible light for 8 h. The yield of CO was only 6.26 μmol·g_{cat}^{-1} over $Mg_{0.4}Cu_{0.6}$-MOF-74 in the dark, which is considerably lower than that under visible light. The result revealed that $Mg_{0.4}Cu_{0.6}$-MOF-74 exhibits an

Table 2. CO_2 Photoreduction of $Mg_{0.4}Cu_{0.6}$-MOF-74 and Mg-MOF-74

samples	product	CO yield/($\mu mol \cdot g_{cat}^{-1}$)	experimental conditions
$Mg_{0.4}Cu_{0.6}$-MOF-74	CO	49.44	X-lamp (8 h)
		6.26	without X-lamp
Mg-MOF	CO	0	X-lamp (8 h)
		0	without X-lamp

excellent CO_2 photoreduction activity. Replacing the Mg of Mg-MOF-74 with Cu can considerably improve the CO_2 photocatalytic activity, which is consistent with the UV and PL analyses.

CONCLUSIONS

Mg_xCu_{1-x}-MOF-74 was successfully constructed at 398 K, 24 h, and in DMF-EtOH-MeOH solvents. The CO_2 adsorption capacity of Mg_xCu_{1-x}-MOF-74 was considerably affected by the temperatures, time, solvents, and Mg/Cu molar ratio. The photostability of Mg_xCu_{1-x}-MOF-74 for CO_2 adsorption was affected by the Mg/Cu molar ratio. The synergistic effect of adjacent Mg and Cu enhanced the CO_2 adsorption capacity and photocatalytic activity. The CO_2 uptake of $Mg_{0.4}Cu_{0.8}$-MOF-74 under the Xe lamp for 24 h was the best, up to 3.52 mmol·g^{-1}. The yield of the photocatalytic reduction of CO_2 to CO was 49.44 $\mu mol \cdot g_{cat}^{-1}$ over $Mg_{0.4}Cu_{0.8}$-MOF-74 under visible light for 8 h. The stability of Mg-MOF-74 was primarily affected by the Mg−O bond on the top of the metal−organic frame (M represents the metal species) and the metal center atoms (Mg). Replacing Mg^{2+} with Cu^{2+} can result in asymmetric defects in the skeleton structure. The distortion and deformation of the coordination environment of Cu^{2+} (i.e., Jahn−Teller effect) lead to the contraction of Mg−O bonds, which enhanced Mg−O bond photostability. The bimetallic strategy is a feasible method for photocatalyst design to achieve remarkable CO_2 adsorption and photocatalytic properties in the future.

ASSOCIATED CONTENT

⑤ Supporting Information

The Supporting Information is available free of charge at https://pubs.acs.org/doi/10.1021/acsomega.2c01717.

> Synthesis details of Mg-MOF-74 and Cu-MOF-74, ICP-AES analysis of S-398-24-A, and SEM, XRD, and CO_2 uptake of Mg_xCu_{1-x}-MOF-74 under three synthesis conditions (temperatures, time, and solvents) (PDF)

AUTHOR INFORMATION

Corresponding Authors

Anning Zhou − *College of Chemistry & Chemical Engineering, Xi'an University of Science and Technology, Xi an 710054, P. R. China*; Email: psu564@139.com

Wenzhen Wang − *College of Chemistry & Chemical Engineering, Xi'an Shiyou University, Xi an 710065, P. R. China*; Email: wzwang@xsyu.edu.cn

Authors

Jie Ling − *College of Chemistry & Chemical Engineering, Xi'an University of Science and Technology, Xi an 710054, P. R. China; College of Coal & Chemical Industry, Shaanxi Energy Institute, Hsienyang 712000, P. R. China*

Xinyu Jia − *College of Chemistry & Chemical Engineering, Xi'an University of Science and Technology, Xi an 710054, P. R. China*

Mengdan Ma − *College of Chemistry & Chemical Engineering, Xi'an University of Science and Technology, Xi an 710054, P. R. China*

Yizhong Li − *College of Chemistry & Chemical Engineering, Xi'an University of Science and Technology, Xi an 710054, P. R. China*

Complete contact information is available at:
https://pubs.acs.org/10.1021/acsomega.2c01717

Notes

The authors declare no competing financial interest.

REFERENCES

(1) Sumida, K.; Rogow, D. L.; Mason, J. A.; McDonald, T. M.; Bloch, E. D.; Herm, Z. R.; Bae, T.-H.; Long, J. R. Carbon Dioxide Capture in Metal-Organic Frameworks. *Chem. Rev.* **2012**, *112*, 724−781.

(2) Trickett, C. A.; Helal, A.; Al-Maythalony, B. A.; Yamani, Z. H.; Cordova, K. E.; Yaghi, O. M. The chemistry of metal-organic frameworks for CO_2 capture, regeneration and conversion. *Nat. Rev. Mater.* **2017**, *2*, 17045.

(3) Hu, Z.; Wang, Y.; Shah, B. B.; Zhao, D. CO_2 Capture in Metal-Organic Framework Adsorbents: An Engineering Perspective. *Adv. Sustain. Syst.* **2019**, *3*, 1800080.

(4) Xue, W.-L.; Wang, L.; Li, Y. K.; Chen, H.; Fu, K. X.; Zhang, F.; He, T.; Deng, Y. H.; Li, J. R.; Wan, C.-Q. Reticular Chemistry for Ionic Liquid-Functionalized Metal-Organic Frameworks with High Selectivity for CO_2. *ACS Sustain. Chem. Eng.* **2020**, *8*, 18558−18567.

(5) (a) Li, Z.; Liu, P.; Ou, C.; Dong, X. Porous Metal-Organic Frameworks for Carbon Dioxide Adsorption and Separation at Low Pressure. *ACS Sustain. Chem. Eng.* **2020**, *8*, 15378−15404. (b) McDonald, T. M.; Liu, W. R. *J. Am. Chem. Soc.* **2012**, *134*, 7056−7065.

(6) McDonald, T. M.; Lee, W. R.; Mason, J. A.; Wiers, B. M.; Hong, C. S.; Long, J. R. Capture of Carbon Dioxide from Air and Flue Gas in the Alkylamine-Appended Metal-Organic Framework mmen-Mg_2(dobpdc). *J. Am. Chem. Soc.* **2012**, *134*, 7056−7065.

(7) Zhu, L.; Liu, X.-Q.; Jiang, H.-L.; Sun, L.-B. Metal-Organic Frameworks for Heterogeneous Basic Catalysis. *Chem. Rev.* **2017**, *117*, 8129−8176.

(8) Wotzka, A.; Dühren, R.; Suhrbier, T.; Polyakov, M.; Wohlrab, S. Adsorptive Capture of CO_2 from Air and Subsequent Direct Esterification under Mild Conditions. *ACS Sustain. Chem. Eng.* **2020**, *8*, 5013−5017.

(9) Yao, H.-F.; Yang, Y.; Liu, H.; Xi, F.-G.; Gao, E.-Q. CPO-27-M as heterogeneous catalysts for aldehyde cyanosilylation and styrene oxidation. *J. Mol. Catal. A: Chem.* **2014**, *394*, 57−65.

(10) Qian, Y.; Zhang, F.; Pang, H. A Review of MOFs and Their Composites-Based Photocatalysts: Synthesis and Applications. *Adv. Funct. Mater.* **2021**, *31*, 2104231.

(11) Zhao, H.; Xia, Q.; Xing, H.; Chen, D.; Wang, H. Construction of Pillared-Layer MOF as Efficient Visible-Light Photocatalysts for Aqueous Cr (VI) Reduction and Dye Degradation. *ACS Sustain. Chem. Eng.* **2017**, *S*, 4449−4456.

(12) Chen, X.; Peng, X.; Jiang, L. B.; Yuan, X. Z.; Fei, J.; Zhang, W. Photocatalytic removal of antibiotics by MOF-derived Ti^{3+}- and

oxygen vacancy-doped anatase/rutile TiO_2 distributed in a carbon matrix. *Chem. Eng. J.* **2022**, *427*, 130945.

(13) Becker, T. M.; Heinen, J.; Dubbeldam, D.; Lin, L.-C.; Vlugt, T. J. H. Polarizable Force Fields for CO_2 and CH_4 Adsorption in M-MOF-74. *J. Phys. Chem. C* **2017**, *121*, 4659–4673.

(14) Dietzel, P. D. C.; Besikiotis, V.; Blom, R. Application of metal-organic frameworks with coordinatively unsaturated metal sites in storage and separation of methane and carbon dioxide. *J. Mater. Chem.* **2009**, *19*, 7362–7370.

(15) Yazaydin, A. O.; Snurr, R. Q.; Park, T. H.; Koh, K.; Liu, J.; Levan, M. D.; Benin, A. I.; Jakubczak, P.; Lanuza, M.; Galloway, D. B.; Low, J. J.; Willis, R. R. Screening of Metal-Organic Frameworks for Carbon Dioxide Capture from Flue Gas Using a Combined Experimental and Modeling Approach. *J. Am. Chem. Soc.* **2009**, *131*, 18198–18199.

(16) Bao, Z.; Yu, L.; Ren, Q.; Lu, X.; Deng, S. Adsorption of CO_2 and CH_4 on a magnesium-based metal organic framework. *J. Colloid Interface Sci.* **2011**, *353*, 549–556.

(17) Alkhatib, I. I.; Garlisi, C.; Pagliaro, M.; Al-Ali, K.; Palmisano, G. Metal-organic frameworks for photocatalytic CO_2 reduction under visible radiation: a review of strategies and applications. *Catal. Today* **2020**, *340*, 209–224.

(18) khalilzadeh, A.; Shariati, A. Fe-N-TiO_2/CPO-Cu-27 nanocomposite for superior CO_2 photoreduction performance under visible light irradiation. *Sol. Energy* **2019**, *186*, 166–174.

(19) Zhao, H.; Wang, X.; Feng, J.; Chen, Y.; Yang, X.; Gao, S.; Cao, R. Synthesis and characterization of Zn_2GeO_4/Mg-MOF-74 composites with enhanced photocatalytic activity for CO_2 reduction. *Catal. Sci. Technol.* **2018**, *8*, 1288–1295.

(20) Wang, M.; Wang, D.; Li, Z. Self-assembly of CPO-27-Mg/TiO_2 nanocomposite with enhanced performance for photocatalytic CO_2 reduction. *Appl. Catal., B* **2016**, *183*, 47–52.

(21) Li, R.; Hu, J.; Deng, M.; Wang, H.; Wang, X.; Hu, Y.; Jiang, H.-L.; Jiang, J.; Zhang, Q.; Xie, Y.; Xiong, Y. Metal-Organic Frameworks: Integration of an Inorganic Semiconductor with a Metal-Organic Framework: A Platform for Enhanced Gaseous Photocatalytic Reactions. *Adv. Mater.* **2014**, *26*, 4907.

(22) Ikreedeegh, R. R.; Tahir, M. A critical review in recent developments of metal-organic-frameworks (MOFs) with band engineering alteration for photocatalytic CO_2 reduction to solar fuels. *J. CO_2 Util.* **2021**, *43*, 101381.

(23) Zuluaga, S.; Fuentes-Fernandez, E. M. A.; Tan, K.; Xu, F.; Li, J.; Chabal, Y. J.; Thonhauser, T. Understanding and Controlling Water Stability of MOF-74. *J. Mater. Chem. A* **2016**, *4*, 5176–5183.

(24) Su, X.; Bromberg, L.; Martis, V.; Simeon, F.; Huq, A.; Hatton, T. A. Post-synthetic functionalization of Mg-MOF-74 with tetraethylenepentamine: structural characterization and enhanced CO_2 adsorption. *ACS Appl. Mater. Interfaces* **2017**, *9*, 11299–11306.

(25) Zhu, X.-W.; Zhou, X.-P.; Li, D. Exceptionally water stable heterometallic gyroidal MOFs: tuning the porosity and hydrophobicity by doping metal ions. *Chem. Commun.* **2016**, *52*, 6513–6516.

(26) Zou, R.; Li, P.-Z.; Zeng, Y.-F.; Liu, J.; Zhao, R.; Duan, H.; Luo, Z.; Wang, J.-G.; Zou, R.; Zhao, Y. Bimetallic Metal-Organic Frameworks: Probing the Lewis Acid Site for CO_2 Conversion. *Small* **2016**, *12*, 2334–2343.

(27) Xie, S.; Qin, Q.; Liu, H.; Jin, L.; Wei, X.; Liu, J.; Liu, X.; Yao, Y.; Dong, L.; Li, B. MOF-74-M (M = Mn, Co, Ni, Zn, MnCo, MnNi, and MnZn) for Low-Temperature NH_3-SCR and In Situ DRIFTS Study Reaction Mechanism. *ACS Appl. Mater. Interfaces* **2020**, *12*, 48476–48485.

(28) Gao, Z.; Liang, L.; Zhang, X.; Xu, P.; Sun, J. Facile One-Pot Synthesis of Zn/Mg-MOF-74 with Unsaturated Coordination Metal Centers for Efficient CO_2 Adsorption and Conversion to Cyclic Carbonates. *ACS Appl. Mater. Interfaces* **2021**, *13*, 61334–61345.

(29) Zurrer, T.; Wong, K.; Horlyck, J.; Lovell, E. C.; Wright, J.; Bedford, N. M.; Han, K.; Scott, J.; Amal, R. Mixed-Metal MOF-74 Templated Catalysts for Efficient Carbon Dioxide Capture and Methanation. *Adv. Funct. Mater.* **2021**, *31*, 2007624.

(30) Jiao, Y.; Morelock, C. R.; Burtch, N. C.; Mounfield, W. P.; Hungerford, J. T.; Walton, K. S. Tuning the Kinetic Water Stability and Adsorption Interactions of Mg-MOF-74 by Partial Substitution with Co or Ni. *Ind. Eng. Chem. Res.* **2015**, *54*, 12408–12414.

(31) Howe, J. D.; Morelock, C. R.; Jiao, Y.; Chapman, K. W.; Walton, K. S.; Sholl, D. S. Understanding Structure, Metal Distribution, and Water Adsorption in Mixed-Metal MOF-74. *J. Phys. Chem. C* **2017**, *121*, 627–635.

(32) Guo, S.-H.; Qi, X.-J.; Zhou, H.-M.; Zhou, J.; Wang, X.-H.; Dong, M.; Zhao, X.; Sun, C.-Y.; Wang, X.-L.; Su, Z.-M. A bimetallic-MOF catalyst for efficient CO_2 photoreduction from simulated flue gas to value added formate. *J. Mater. Chem. A* **2020**, *8*, 11712–11718.

(33) Li, X.; He, C.; Zheng, J.; Wu, D.; Duan, Y.; Li, Y.; Rao, P.; Tang, B.; Rui, Y. Flocculent Cu Caused by the Jahn-Teller Effect Improved the Performance of Mg-MOF-74 as an Anode Material for Lithium-Ion Batteries. *ACS Appl. Mater. Interfaces* **2020**, *12*, 52864–52872.

(34) Ahmadzadeh, Z.; Javad, M.; Morteza, R. Cu-MOF: an efficient heterogeneous catalyst for the synthesis of symmetric anhydrides via the C-H bond activation of aldehydes. *RSC Adv.* **2018**, *8*, 24203–24208.

(35) Sanz, R.; Martínez, F.; Orcajo, G.; Wojtas, L.; Briones, D. Synthesis of a honeycomb-like Cu-based metal-organic framework and its carbon dioxide adsorption behaviors. *Dalton Trans.* **2013**, *42*, 2392–2398.

(36) Sun, H.; Ren, D.; Kong, R.; Wang, D.; Jiang, H.; Tan, J.; Wu, D.; Chen, S.; Shen, B. Tuning 1-hexene/n-hexane adsorption on MOF-74 via constructing Co-Mg bimetallic frameworks. *Microporous Mesoporous Mater.* **2019**, *284*, 151–160.

(37) Hu, J.; Chen, Y.; Zhang, H.; Chen, Z. Controlled syntheses of Mg-MOF-74 nanorods for drug delivery. *J. Solid State Chem.* **2021**, *294*, 121853.

(38) Li, H.; Yang, Z.; Lu, S.; Su, L.; Wang, C.; Huang, J.; Zhou, J.; Tang, J.; Huang, M. Nano-porous bimetallic CuCo-MOF-74 with coordinatively unsaturated metal sites for peroxymonosulfate activation to eliminate organic pollutants: Performance and mechanism. *Chemosphere* **2021**, *273*, 129643.

(39) Kahr, J.; Morris, R. E.; Wright, P. A. Post-synthetic incorporation of nickel into CPO-27(Mg) to give materials with enhanced permanent porosity. *CrystEngComm* **2013**, *15*, 9779.

(40) Tan, K.; Zuluaga, S.; Gong, Q.; Canepa, P.; Wang, H.; Li, J.; Chabal, Y. J.; Thonhauser, T. Water Reaction Mechanism in Metal Organic Frameworks with Coordinatively Unsaturated Metal Ions: MOF-74. *Chem. Mater.* **2014**, *26*, 6886–6895.

(41) Romero-Muñiz, C.; Gavira-Vallejo, J. M.; Merkling, P. J.; Calero, S. Impact of Small Adsorbates in the Vibrational Spectra of Mg- and Zn-MOF-74 Revealed by First-Principles Calculations. *ACS Appl. Mater. Interfaces* **2020**, *12*, 54980–54990.

(42) Abooali, D.; Soleimani, R.; Rezaei-Yazdi, A. Modeling CO_2 absorption in aqueous solutions of DEA, MDEA, and DEA+MDEA based on intelligent methods. *Sep. Sci. Technol.* **2020**, *55*, 697–707.

(43) Kondrashova, D.; Valiullin, R. Freezing and Melting Transitions under Mesoscalic Confinement: Application of the Kossel-Stranski Crystal-Growth Model. *J. Phys. Chem. C* **2015**, *119*, 4312–4323.

(44) Cui, C.; Ren, H.; Jiao, Q. Solubility Measurement and Correlation for ε-2,4,6,8,10,12-Hexanitro-2,4,6,8,10,12-hexaazaisowurtzitane in Different Alkanes/Aromatic Hydrocarbon+Ethyl Acetate Binary Solvents at Temperatures of between 283.15 and 323.15 K. *J. Chem. Eng. Data* **2018**, *63*, 3097–3106.

(45) Shen, F.; Lv, P.; Sun, C.; Zhang, R.; Pang, S. The Crystal Structure and Morphology of 2,4,6,8,10,12-Hexanitro-2,4,6,8,10,12-hexaazaisowurtzitane (CL-20) p-Xylene Solvate: A Joint Experimental and Simulation Study. *Molecules* **2014**, *19*, 18574–18589.

(46) Ge, Y.; Wang, K.; Li, H.; Tian, Y.; Wu, Y.; Lin, Z.; Lin, Y.; Wang, Y.; Zhang, J.; Tang, B. An Mg-MOFs based multifunctional medicine for the treatment of osteoporotic pain. *Mater. Sci. Eng., C* **2021**, *129*, 112386.

(47) Chen, C.; Feng, X.; Zhu, Q.; Dong, R.; Yang, R.; Cheng, Y.; He, C. Microwave-Assisted Rapid Synthesis of Well-Shaped MOF-74 (Ni) for CO_2 Efficient Capture. *Inorg. Chem.* **2019**, *58*, 2717−2728.

(48) Kadi, M. W.; El Salam, H. M. A.; Zaki, T.; Mohamed, R. M. Adsorption of carbon dioxide on $Cu_xMg_y(BTC)_2$ MOFs: influence of Cu/Mg ratio. *J. Nanopart. Res.* **2020**, *22*, 143.

(49) Tabatabaei, N.; Dashtian, K.; Ghaedi, M.; Sabzehmeidani, M. M.; Ameri, E. Novel visible light-driven Cu-based MOFs/Ag_2O composite photocatalysts with enhanced photocatalytic activity toward the degradation of orange G: their photocatalytic mechanism and optimization study. *New J. Chem.* **2018**, *42*, 9720.

(50) Xu, H.; Xie, J.; Jia, W.; Wu, G.; Cao, Y. The formation of visible light-driven Ag/Ag_2O photocatalyst with excellent property of photocatalytic activity and photocorrosion inhibition. *J. Colloid Interface Sci.* **2018**, *516*, 511−521.